Linear Stability Analysis of an INDI Pitch-Rate Controller under Model Mismatch for a Tilt-Rotor VTOL UAV

Lorenzo Schenk
IDSC
ETH Zurich
Zurich, Switzerland
lschen@ethz.ch

Guillaume Ducard
I3S Laboratory
Univ. Côte d'Azur
Sophia Antipolis, France
guillaume.ducard@univ-cotedazur.fr

Christopher Onder
IDSC
ETH Zurich
Zurich, Switzerland
onder@idsc.mavt.ethz.ch

arXiv:2607.16471v1 [cs.RO] 17 Jul 2026

***Abstract*—Incremental Nonlinear Dynamic Inversion (INDI) is attractive for unmanned aerial vehicle (UAV) flight control because it reduces dependence on a full aerodynamic model while retaining strong disturbance-rejection capability. For a tilt-rotor vertical takeoff and landing (VTOL) architecture, however, the admissible model-mismatch range of the fast inner loop is still not characterized analytically in a parameter-explicit way. This paper isolates the pitch-rate/elevon subchannel of an existing cascaded INDI controller and studies its linear stability under model mismatch. A closed-form fifth-order transfer function is derived for the full controller–estimator–actuator–plant interconnection, and stability is characterized through the Routh–Hurwitz criterion over a parameterized linear model. Two representative three-parameter sweeps produce interpretable stability regions. Based on these feasibility maps, two uncertainty-aware tuning procedures are proposed: a robustness-oriented design that maximizes a weighted worst-case combination of gain margin and phase margin, and a performance-oriented design that maximizes worst-case closed-loop bandwidth subject to margin constraints. The results show that actuator lag and inertia mismatch are comparatively benign at nominal gain, whereas control-effectiveness mismatch, particularly a sign error in the allocation, is the most dangerous destabilizing factor, leading to concrete tuning recommendations for conservative and aggressive operating conditions.**

***Index Terms*—INDI, tilt-rotor UAV, pitch stability, model mismatch, Routh–Hurwitz, robust control, parameter optimization, design recommendation**

I. Introduction

A. INDI: Significance and Stability Challenges

Incremental Nonlinear Dynamic Inversion (INDI) has emerged as a leading flight-control approach for both rotary- and fixed-wing UAVs [1]–[3]. Unlike classical nonlinear dynamic inversion (NDI) [4]–[6], which relies on a more complete model cancellation, INDI uses measured angular acceleration together with a local control-effectiveness model to generate incremental control commands [2]. This substantially reduces dependence on a full aerodynamic model and often improves disturbance rejection in practice [1], but the closed-loop stability margin still depends on how actuator, filtering, inertia, and effectiveness mismatch enter the implemented loop. Quantifying the admissible mismatch range is therefore still necessary, especially across wide flight envelopes.

Recent work has also broadened the field through a comprehensive survey of INDI components, stability, and robustness [7] and through adaptive INDI with guaranteed stability for aerial manipulators under varying inertia and control-effectiveness conditions [8]. Nevertheless, for aircraft inner loops, analytical treatments still either rely on simplified single-lag plant models [1], address related robustness questions without providing a parameter-explicit Routh characterization of the fast pitch-rate inner loop [9], or assess stability numerically and empirically [10]. A closed-form mismatch-explicit Routh–Hurwitz analysis of the pitch-rate loop of a tilt-rotor VTOL is still missing.

B. Contributions

This paper makes the following contributions:

1) A closed-form, fifth-order transfer function is derived for the pitch-rate/elevon subchannel of the cascaded INDI controller [2], explicitly accounting for actuator lag, estimator filtering, and inverse control allocation.
2) The Routh–Hurwitz criterion is used to obtain interpretable stability conditions and to visualize representative three-parameter stability regions.
3) Two uncertainty-aware tuning procedures are formulated on top of the Routh-feasible set: a robustness-oriented design maximizing a weighted worst-case combination of gain and phase margin, and a performance-oriented design maximizing worst-case closed-loop bandwidth subject to margin constraints.

The analysis isolates the pitch-rate/elevon subchannel from the cascaded INDI inner loop of [2]. This channel is selected because the longitudinal transition maneuver considered here is dominated by pitch dynamics: acceleration from hover to forward flight requires a sustained pitch-down command that drives the elevon toward its deflection limits, making the pitch

*This work was supported by the French government through the France 2030 investment plan managed by the National Research Agency (ANR), as part of the Initiative of Excellence Université Côte d'Azur under reference number ANR-15-IDEX-01.

channel the most likely to become unstable under effectiveness mismatch. The reduction to the standalone pitch-rate loop is exact at nominal gain because, under the inherited controller architecture of [2], the attitude-control and control-allocation blocks produce identical elevon commands at the nominal operating point; deviations from this equivalence constitute part of the model mismatch studied here. The resulting linear stability certificate is therefore a local inner-loop result, not a full-envelope MIMO guarantee for aggressive coupled flight or saturated actuation. The remainder of the paper is structured as follows: Section II derives the linear model, Section III characterizes its stability, and Section IV presents the optimization results and design guidelines.

II. System and Controller

A. Aircraft Pitch Model

Small-perturbation longitudinal dynamics about a trimmed flight condition reduce to the single-axis pitch equation [6]:

$$I_{yy,m}\,\dot{q} = M_m\,\delta - d_q\,q, \tag{1}$$

where q is the pitch rate, δ the elevon deflection, $M_m \equiv \partial M/\partial\delta$ the pitch-moment effectiveness, $d_q > 0$ the aerodynamic pitch-rate damping (stabilizing), and $I_{yy,m}$ the true moment of inertia. Defining

$$K_q \triangleq \frac{M_m}{I_{yy,m}}, \qquad \omega_p \triangleq \frac{d_q}{I_{yy,m}}, \tag{2}$$

the plant transfer function is $G_{\text{plane}}(s) = K_q/(s+\omega_p)$. Actuator dynamics are modeled as a first-order lag system:

$$G_{\text{act}}(s) = \frac{1}{1+\tau_{\text{act}}\,s}. \tag{3}$$

In the stable-parameter-range analysis of Section IV-A, $d_q = 0$ is used, giving the integrating plant $G_{\text{plane}}(s) = K_q/s$. Over the physically meaningful parameter range considered here and with the nominal sign convention preserved, positive aerodynamic damping adds non-negative corrections to the intermediate characteristic-polynomial coefficients (cf. Table II) and relaxes, rather than tightens, the observed Routh conditions. We therefore use $d_q = 0$ as a conservative baseline in the stability sweeps, whereas the performance optimization in Section IV-B reintroduces a non-zero d_q explicitly.

B. INDI Pitch-Rate Controller

The reduced pitch-rate controller structure, shown in Fig. 1, follows the inherited architecture of [2] and consists of four interconnected blocks: a proportional error feedback, a pitch-rate estimator, an inverse control allocation, and a low-pass filter chain.

Proportional path. The tracking error $e = q_{\text{ref}} - q_m$ is multiplied by the proportional gain k_p. The rate-estimate branch subtracts the low-pass-filtered estimate of $\dot{q}$, giving the incremental acceleration demand:

$$\Delta\dot{q}(s) = k_p\,e(s) - \underbrace{\frac{k_{\text{LP}}\,s}{s+k_{\text{LP}}}\,q_m(s)}_{\dot{q}_{LP}(s)}. \tag{4}$$

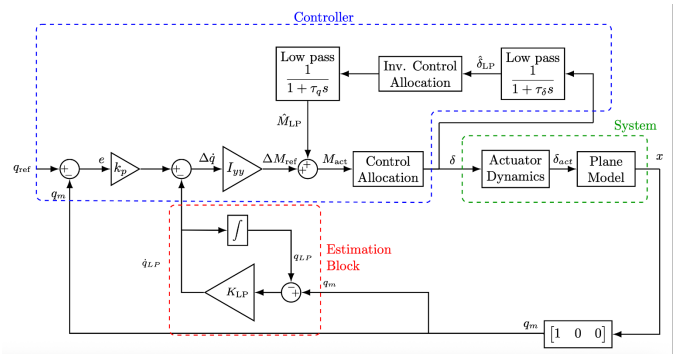

Fig. 1. INDI pitch-rate loop derived from the inner-loop architecture of [2]. Blue: Controller; red: Estimation Block; green: System (actuator + plant).

Moment reference. The increment in pitch moment ΔM_{ref} is obtained by multiplying $\Delta\dot{q}$ by the controller moment of inertia estimate $I_{yy,c}$.

Moment Estimator (feedback compensation). The estimated moment $\hat{M}_{LP}$ is reconstructed from the commanded elevon deflection δ through two cascaded first-order filters,

$$F(s) = \frac{\hat{M}_{LP}(s)}{M_{act}(s)} = \frac{1}{(1+\tau_q s)(1+\tau_\delta s)}. \tag{5}$$

In the matched implementation considered here, the same control-effectiveness parameter M_d is used in both the control allocation $\Delta\delta = \Delta M_{\text{ref}}/M_d$ and the estimator-side moment reconstruction. The internal estimator loop therefore reduces to

$$B(s) = \frac{M_{\text{act}}(s)}{\Delta M_{\text{ref}}(s)} = \frac{1}{1-F(s)}. \tag{6}$$

Model mismatch is introduced only through the difference between the assumed effectiveness M_d and the true aircraft effectiveness M_m.

Nominal time-alignment. From Fig. 1, the low-pass branch acting on the measured pitch rate q_m is

$$\frac{k_{\text{LP}}}{s+k_{\text{LP}}} = \frac{1}{1+\tau_q s}, \qquad \tau_q \triangleq \frac{1}{k_{\text{LP}}},$$

which is aligned with the estimator filter when $k_{\text{LP}} = 1/\tau_q$. In the same way, the reconstruction filter $1/(1+\tau_\delta s)$ matches the actuator dynamics $1/(1+\tau_{\text{act}}s)$ when $\tau_\delta = \tau_{\text{act}}$. These relations define the nominal time-alignment conditions

$$k_{\text{LP}} = \frac{1}{\tau_q}, \qquad \tau_\delta = \tau_{\text{act}}. \tag{7}$$

The quantities k_{LP}, τ_q, and τ_δ are design choices, whereas τ_{act} is a fixed physical parameter. Satisfying (7) ensures that the reconstructed moment $\hat{M}_{LP}$ and angular-acceleration estimate $\dot{q}_{LP}$ are based on the same delayed actuator signal; otherwise, phase mismatch is introduced into the incremental cancellation path [9]. Section IV-A therefore varies τ_q, τ_δ, and k_{LP} independently to assess sensitivity to departures from nominal alignment.

TABLE I
NOMINAL PARAMETER VALUES AT THE $V_a = 20$ M/S FIXED-WING TRIM POINT.

Symbol	Value	Unit	Origin
System parameters			
$I_{yy,m}$	0.025	kg m^2	Physical airframe inertia
τ_{act}	0.05	s	First-order servo model
M_m	≈ -8.4	N m/rad	at V_a=20 m/s from [2]
d_q	≈ 3.92	N m s/rad	$-\frac{1}{4}\rho V_a^2 S\bar{c}^2 C_{mq}$ [2]
Controller parameters (nominal = matched)			
$I_{yy,c}$	$= I_{yy,m}$	kg m^2	Matched inertia
M_d	$= M_m$	N m/rad	Matched effectiveness
k_p	20	rad/s	Bandwidth target [2]
τ_q	0.004	s	Estimator corner
k_{LP}	$= \frac{1}{\tau_q} = 250$	rad/s	Condition (7)
τ_δ	$= \tau_{\text{act}} = 0.05$	s	Condition (7)

C. Closed-Loop Transfer Function

The total effective plant seen by the proportional controller is $P(s) = G_{\text{plane}}(s) \cdot G_{\text{act}}(s) \cdot (1/M_d) \cdot B(s)$. Here $P(s)$ is the forward map from the incremental moment reference to the measured pitch rate, i.e. $q_m(s) = P(s)\Delta M_{\text{ref}}(s)$. Since

$$\Delta M_{\text{ref}}(s) = I_{yy,c}\left[k_p(q_{\text{ref}}(s) - q_m(s)) - \frac{k_{LP}s}{s+k_{LP}} q_m(s)\right],$$

substitution gives

$$q_m = P(s)I_{yy,c}k_p q_{\text{ref}} - P(s)I_{yy,c}\left(k_p + \frac{k_{LP}s}{s+k_{LP}}\right) q_m.$$

Collecting the q_m-terms yields (8). The closed-loop pitch-rate transfer function is

$$\frac{q_m(s)}{q_{\text{ref}}(s)} = \frac{P(s)\, I_{yy,c}\, k_p}{1 + P(s)\, I_{yy,c}\left(k_p + \frac{k_{\text{LP}}\, s}{s+k_{\text{LP}}}\right)}. \tag{8}$$

Expanding (8) with $G_{\text{plane}}(s) = K_q/s$ yields a fifth-order characteristic polynomial with coefficients that depend explicitly on $\{k_p,\, k_{\text{LP}},\, I_{yy,c},\, \tau_{\text{act}},\, \tau_q,\, \tau_\delta,\, M_d,\, K_q\}$.

D. Nominal Parameter Values

Table I collects the nominal values used throughout the analysis. System parameters are fixed by the airframe and operating point; controller parameters are design choices initialized to match the physical plant.

The pitch-moment effectiveness $M_m = \bar{q}Sc\, C_{m\delta}$ is computed from the dynamic pressure $\bar{q} = \frac{1}{2}\rho V_a^2$, wing area S, chord c, and the pitch-moment derivative $C_{m\delta}$ [6]. At $V_a = 20\,\text{m/s}$ this gives $M_m \approx -8.4\,\text{N m/rad}$ under the adopted NED nose-down sign convention. This signed convention is used throughout, so $K_q = M_m/I_{yy,m}$ and M_d retain their physical sign; in the matched nominal case M_d and M_m have the same sign, whereas a sign error corresponds to M_d crossing zero and reversing relative to M_m. The aerodynamic pitch-rate damping $d_q \approx 3.92\,\text{N m s/rad}$ is computed from the same trim condition. The controller parameters $I_{yy,c}$ and M_d are initialized to their physical counterparts, and k_{LP} and τ_δ follow directly from the time-alignment condition (7). Throughout the stability analysis in IV-A, parameter perturbations are expressed as percentages of their signed nominal values; for M_d in particular, $M_{d,\text{nom}} < 0$ under the adopted NED convention, so that a perturbation crossing 0% corresponds to an allocation-sign reversal, identified in Section IV-A as the most dangerous destabilizing mode.

III. STABILITY ANALYSIS

A. Parameter Space and Model Mismatch

The closed-loop characteristic polynomial depends on the system model and controller parameters:

$$\underbrace{M_m, I_{yy,m}, \tau_{\text{act}}, d_q}_{\text{system parameters}} \qquad \underbrace{M_d, k_p, I_{yy,c}, \tau_q, \tau_\delta, k_{LP}}_{\text{controller parameters}}$$

The stability maps consider two representative three-parameter subspaces: Sweep A varies $\{M_d, \tau_{\text{act}}, k_p\}$ and Sweep B varies $\{I_{yy,c}, k_p, \tau_\delta\}$, while all remaining quantities are fixed at their nominal values. In the optimization, the tunable controller vector is

$$\theta = \{I_{yy,c}, M_d, k_p, \tau_q, \tau_\delta, k_{LP}\},$$

whereas plant uncertainty enters through multiplicative perturbations of the physical parameters, as detailed in Section IV-B.

B. Routh–Hurwitz Stability Criterion

For a given parameter tuple $\boldsymbol{\theta}$, the characteristic polynomial of (8) is formed and the Routh array is evaluated.

Table II makes clear that positive aerodynamic damping enters as additive corrections to the intermediate coefficients, which explains why the undamped case is a conservative baseline, even though the full stability decision is still made through the complete Routh array.

TABLE II
CHARACTERISTIC POLYNOMIAL COEFFICIENTS: UNDAMPED BASELINE ($\omega_p = 0$) VERSUS DAMPED FORM. HERE $G_{MM} = I_{yy,c}K_q/M_d$, $T_s = \tau_q + \tau_\delta$, AND $T_p = \tau_q\tau_\delta$. POSITIVE AERODYNAMIC DAMPING ADDS ONLY THE LISTED CORRECTIONS δC_i, WITH $\delta C_5 = \delta C_0 = 0$.

Coeff.	Undamped $C_i^{(0)}$ ($\omega_p = 0$)	Full $C_i = C_i^{(0)} + \delta C_i$
C_5	$\tau_{\text{act}} T_p$	unchanged
C_4	$\tau_{\text{act}} T_s + T_p(1 + \tau_{\text{act}} k_{lp})$	$+\,\omega_p \tau_{\text{act}} T_p$
C_3	$\tau_{\text{act}} k_{lp} T_s + T_s + T_p k_{lp} + G_{MM} T_p(k_p + k_{lp})$	$+\quad \omega_p[\tau_{\text{act}} T_s \;+\; T_p(1 \;+\; \tau_{\text{act}} k_{lp})]$
C_2	$k_{lp} T_s + G_{MM}[k_p k_{lp} T_p + (k_p + k_{lp}) T_s]$	$+\quad \omega_p[T_s(1 \;+\; \tau_{\text{act}} k_{lp}) \;+\; k_{lp} T_p]$
C_1	$G_{MM}[(k_p \;+\; k_{lp}) \;+\; k_p k_{lp} T_s]$	$+\,\omega_p\, k_{lp} T_s$
C_0	$G_{MM} k_p k_{lp}$	unchanged

To interpret the sampled Routh boundary, we inspected which first-column entry becomes non-positive first along the numerically observed stability frontier [11]. Two recurring

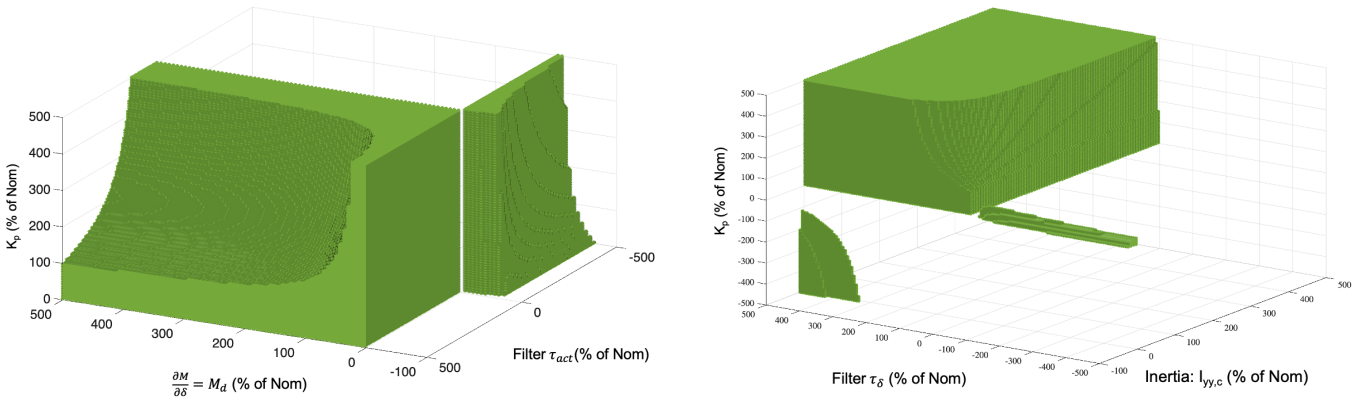

Fig. 2. Stable parameter regions. Green voxels indicate parameter combinations for which all first-column entries of the Routh array are strictly positive, i.e. the closed-loop system is asymptotically stable; the absence of voxels denotes instability. Left (**Sweep A**): $\{M_d,\ \tau_{\text{act}},\ k_p\}$. Right (**Sweep B**): $\{I_{yy,c},\ k_p,\ \tau_\delta\}$. Axes in percent of nominal; for M_d, percentages are relative to the signed nominal value $M_{d,\text{nom}} < 0$; crossing 0% corresponds to an allocation-sign reversal. Each sweep contains a small disconnected stable island at negative k_p (visible in both panels)

mechanisms dominate. First, the admissible proportional action is limited by an effective loop-gain combination,

$$\hat{K} \triangleq \frac{K_q I_{yy,c} k_p}{M_d},$$

so smaller $|M_d|$, larger k_p, or larger $I_{yy,c}$ push the loop toward instability. Second, the actuator and filter dynamics contribute through the corner frequencies $\omega_a = 1/\tau_{act}$, $\omega_q = 1/\tau_q$, and $\omega_\delta = 1/\tau_\delta$, so increasing any of these time constants reduces the admissible gain range. For compactness we summarize these two recurring trends by the heuristic relations

$$\hat{K} < f_1(\omega_a, \omega_q, \omega_\delta) \tag{9}$$

$$\omega_a \omega_q \omega_\delta > f_2(\hat{K}) \tag{10}$$

where f_1 and f_2 are induced by the corresponding Routh first-column expressions. These relations are descriptive summaries of the sampled boundary, not reduced exact stability tests; all numerical stability decisions in this paper are still made using the full fifth-order Routh criterion.

Condition (9) bounds the effective loop gain: underestimating M_d inflates $\hat{K}$ and drives the system toward instability. Condition (10) requires the product of corner frequencies to exceed a threshold set by $\hat{K}$: excessive lag from the actuator, estimator, or alignment filter reduces this product and shrinks the stable gain range, represented in the green volume.

C. Stable Volume Visualization

Two complementary three-dimensional parameter sweeps are performed, shown in Fig. 2. For each sweep, a dense Cartesian grid of 150^3 points is evaluated over the normalized range $[-500\%, 500\%]$ on each axis. At every grid point, the full fifth-order characteristic polynomial is formed, the complete Routh array is constructed, and the point is labeled stable if and only if all first-column entries are strictly positive. The voxel plots therefore represent sampled feasibility sets rather than fitted surfaces.

Sweep A varies $\{M_d, \tau_{\text{act}}, k_p\}$ and **Sweep B** varies $\{I_{yy,c}, k_p, \tau_\delta\}$, with all remaining parameters held at their nominal values. A small disconnected stable region is also visible for negative k_p in both sweeps; this branch is noted for completeness but is not pursued further because the present study focuses on practically relevant positive-gain tuning.

IV. Results and Design Recommendations

A. Stable Parameter Ranges

Sweep A (Fig. 2, left) shows a stable region whose admissible k_p ceiling rises monotonically as M_d decreases from 500% of nominal toward 0%, then vanishes abruptly when M_d crosses zero. Condition (9) alone would predict the ceiling should rise with M_d (since larger $|M_d|$ reduces $\hat{K}$); the plot shows the opposite. The reason is that M_d enters the gain-loaded characteristic-polynomial terms through $G_{MM} = I_{yy,c}K_q/M_d$. At large M_d, G_{MM} is small, which weakens C_1 and C_3 and makes the admissible k_p ceiling mainly set by the actuator–filter time scales rather than by $\hat{K}$ alone. As M_d decreases, G_{MM} grows, strengthening these terms and raising the admissible ceiling. Larger τ_{act} uniformly lowers this ceiling at all M_d, consistent with condition (10): larger τ_{act} reduces ω_a and tightens the corner-frequency product. Equivalently, the actuator then delivers the requested moment with excessive delay, so increasing k_p mainly increases phase lag rather than useful pitch-rate correction. When M_d crosses zero, the allocation sign reverses and INDI becomes positive feedback, which means that in practice the commanded incremental moment is applied with the wrong sign. No positive k_p can stabilize this, and the entire positive-gain stable region vanishes.

Sweep B (Fig. 2, right) shows a large stable block across most of the physically meaningful region ($\tau_\delta > 0$, $I_{yy,c} > 0$), with the k_p ceiling decreasing as both τ_δ and $I_{yy,c}$ simultaneously approach 0% of nominal. Both dominant conditions predict the opposite: $I_{yy,c} \to 0^+$ reduces $\hat{K}$ (relaxing condition (9)) and $\tau_\delta \to 0^+$ increases ω_δ (relaxing condition (10)).

The instability arises from a simultaneous collapse of the polynomial structure: $\tau_\delta \to 0^+$ makes $C_5 = \tau_{\text{act}}\tau_q\tau_\delta \to 0$, while $I_{yy,c} \to 0^+$ drives $G_{MM} \to 0$ and weakens the gain-carrying low-order terms C_0 and C_1. This boundary is therefore captured only by the full Routh test, not by the two heuristic summaries alone. Physically, the problem is the simultaneous loss of two stabilizing mechanisms: $\tau_\delta \to 0$ removes one reconstruction dynamic from the estimator path, while $I_{yy,c} \to 0$ removes the low-frequency corrective moment generated from the pitch-rate error. Note that $\tau_\delta \to 0$ also constitutes a severe violation of the time-alignment condition (7), confirming that operating far below $\tau_\delta = \tau_{\text{act}}$ is not safe despite the apparent relaxation of the heuristic lag condition.

B. Uncertainty-Aware Tuning

Robustness optimization ($d_q = 0$, $\pm 25\%$). The uncertainty set $\mathcal{C}$ is defined by $\pm 25\%$ perturbations of the three uncertain plant parameters $\{\tau_{\text{act}},\, M_m,\, I_{yy,m}\}$, giving 8 vertex cases $c \in \mathcal{C}$. The optimization is carried out on these extreme cases only, so the resulting solution is the best one over the tested vertices, not a formal optimum over the full interior of the uncertainty box. The objective is the weighted worst-case combination of gain and phase margin:

$$\max_{\boldsymbol{\theta}} \min_{c\in\mathcal{C}} \Big[0.5\, G_m(\boldsymbol{\theta}, c) + 0.5\, P_m(\boldsymbol{\theta}, c)\Big]. \tag{11}$$

G_m and P_m are computed from the open-loop transfer function associated with (8). Setting $d_q = 0$ makes this study conservative with respect to positive aerodynamic damping over the parameter range considered.

Performance optimization ($d_q > 0$, $\pm 10\%$). Aerodynamic damping is included as a fourth uncertain parameter, giving 16 corners $c \in \mathcal{C}$ ($\pm 10\%$ on each of the four parameters). The objective is worst-case bandwidth subject to margin constraints:

$$\max_{\boldsymbol{\theta}} \min_{c\in\mathcal{C}} \omega_{\text{BW}}(\boldsymbol{\theta}, c), \tag{12}$$

$$\text{s.t.} \quad 45^\circ \le P_m(\boldsymbol{\theta}, c) \le 60^\circ,\; G_m(\boldsymbol{\theta}, c) \ge 6\,\text{dB},\; \forall c \in \mathcal{C}.$$

Here ω_{BW} denotes the first $-3\,\text{dB}$ crossing of the closed-loop transfer magnitude $|T(j\omega)|$, with $T(s) = q_m(s)/q_{\text{ref}}(s)$. The 6 dB gain floor provides a standard $2\times$ gain safety factor.

Both problems are solved by exhaustive grid search over the Routh-feasible controller grid

$$\Theta = \Theta_{I_{yy,c}} \times \Theta_{M_d} \times \Theta_{k_p} \times \Theta_{\tau_q} \times \Theta_{\tau_\delta} \times \Theta_{k_{LP}}.$$

Algorithm 1 summarizes the search procedure. This grid is distinct from the three-parameter visualization sweeps of Section III-C, which only display representative slices of the stability boundary.

Algorithm 1: Uncertainty-Aware Controller Parameter Search

Require: Uncertainty set $\mathcal{C}$, parameter grid Θ, objective
Ensure: Optimal parameter set $\boldsymbol{\theta}^*$
1: Evaluate the Routh criterion for all $\boldsymbol{\theta} \in \Theta$; retain Θ_{stable}
2: **for** each $\boldsymbol{\theta} \in \Theta_{\text{stable}}$ **do**
3: Compute Routh feasibility, G_m, P_m, and ω_{BW} for all $c \in \mathcal{C}$
4: Evaluate objective (11) or (12)
5: **end for**
6: Return $\boldsymbol{\theta}^* = \arg\max_{\boldsymbol{\theta}\in\Theta_{\text{stable}}}$ objective

In the implementation, the Routh–Hurwitz test is used as a cheap pre-filter before gain-margin, phase-margin, and bandwidth evaluations are performed at the uncertainty corners. With N grid points per controller parameter and n_c uncertain plant parameters evaluated at box vertices, the uniform search scales as $\mathcal{O}(N^6 \cdot 2^{n_c})$. For higher-dimensional problems, the same code structure could be made more scalable by replacing the uniform grid with coarse-to-fine refinement around Routh-feasible or Pareto-relevant regions.

C. Recommended Parameter Sets

The two optimal sets do not follow the same structural logic; rather, they reflect two different operating objectives under two different uncertainty descriptions. The robustness-optimal set drives the loop into a conservative regime by choosing a very small k_p, fast filters, and a large M_d, thereby reducing the effective loop gain and producing large stability margins. The performance-optimal set, by contrast, pushes several parameters toward the edge of the admissible search box and should therefore be interpreted as a boundary-seeking high-bandwidth candidate within the chosen grid, not as evidence of the same tuning pattern. The clearest common feature between the two solutions is a small τ_q, which indicates that a fast rate-estimation path is beneficial in both formulations.

TABLE III
OPTIMIZED PARAMETER SETS RELATIVE TO NOMINAL. ($\pm 25\%$, d_q=0): INDEPENDENT $\pm 25\%$ VARIATIONS OF $\{\tau_{\text{ACT}}, M_m, I_{yy,m}\}$, d_q FIXED AT ZERO. ($\pm 10\%$, d_q>0): $\pm 10\%$ VARIATIONS OF ALL FOUR PARAMETERS INCLUDING $d_q > 0$.

Param.	**Robustness** ($\pm 25\%$, d_q=0)	**Performance** ($\pm 10\%$, d_q>0)
$I_{yy,c}^{\text{opt}}$	$0.05 \cdot I_{yy,c}^{\text{nom}}$	$4.29 \cdot I_{yy,c}^{\text{nom}}$
$k_{\text{LP}}^{\text{opt}}$	$0.75 \cdot k_{\text{LP}}^{\text{nom}}$	$5.0 \cdot k_{\text{LP}}^{\text{nom}}$
τ_δ^{opt}	$0.05 \cdot \tau_\delta^{\text{nom}}$	$2.88 \cdot \tau_\delta^{\text{nom}}$
k_p^{opt}	$0.02 \cdot k_p^{\text{nom}}$	$1.45 \cdot k_p^{\text{nom}}$
τ_q^{opt}	$0.05 \cdot \tau_q^{\text{nom}}$	$0.05 \cdot \tau_q^{\text{nom}}$
M_d^{opt}	$5.0 \cdot M_d^{\text{nom}}$	$0.05 \cdot M_d^{\text{nom}}$

The **robustness-optimal** set achieves guaranteed gain margins above $\approx 30\,\text{dB}$ and phase margins near 60° across all eight corners, but sacrifices performance at the cost of a slow overdamped step response (settling time $\approx 2.5\,\text{s}$) (see Fig. 3, left), which makes it unsuitable as the nominal tuning for agile UAV operation. Its value lies instead in serving as a *conservative stability certificate*: a verified safe operating point that can be used as a validated baseline when plant parameters are poorly characterized. In deployment, this set is therefore best interpreted as a low-confidence fallback tuning, for example during early flight testing or after suspected effectiveness

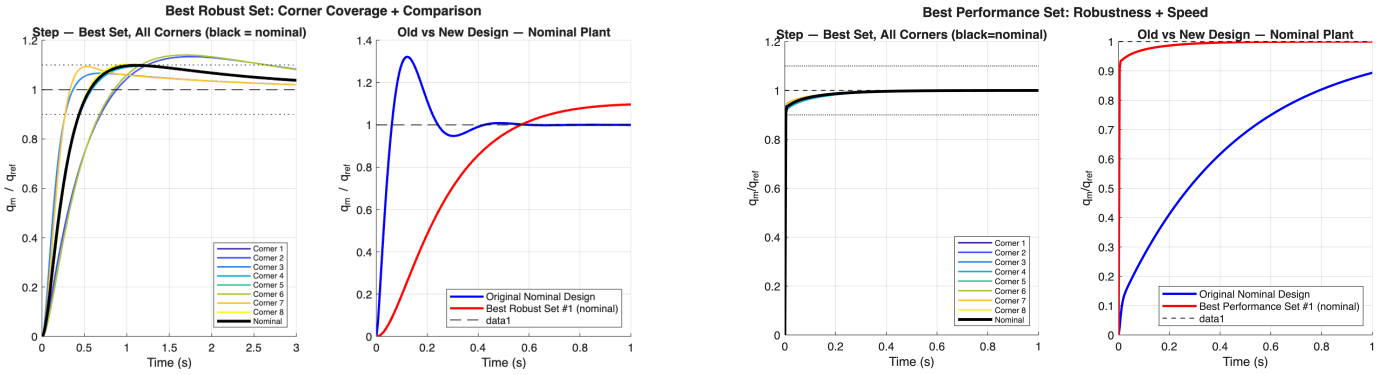

Fig. 3. Step responses for the two optimal parameter sets. Black & red = nominal plant; colored lines = all uncertainty corners. Left: robustness-optimal set ($\pm 25\%$, d_q=0): tight overdamped bundle, settling in ≈ 2.5 s, compared to the original design (right sub-panel). Right: performance-optimal set ($\pm 10\%$, d_q>0): all corners settle within ≈ 0.1 s, $\approx 4\times$ faster than the original design on the nominal plant.

degradation. Agility can then be recovered by moving toward the performance-oriented design when the uncertainty bounds are tighter and positive aerodynamic damping is sufficiently characterized.

The **performance-optimal** set achieves a substantially larger worst-case closed-loop bandwidth than the nominal design while satisfying the $[45°, 60°]$ phase-margin window and the 6 dB gain floor. In the current numerical sweep, the largest qualified bandwidth values are finite and occur around $\omega_{BW} \approx 1.6 \times 10^3\,\mathrm{rad/s}$. This high value indicates that, within the linear model and the imposed gain/phase-margin constraints, the modeled actuator lag, filtering, and mismatch are not the active bandwidth-limiting factors for this parameter combination. In practice, the limiting mechanisms would be hard elevon deflection and rate limits, sampling delay, sensor bandwidth, and structural constraints, which are not included in (12). The corresponding step responses in Fig. 3 are markedly faster than the nominal design, but this improvement requires tighter uncertainty bounds and knowledge of nominal d_q.

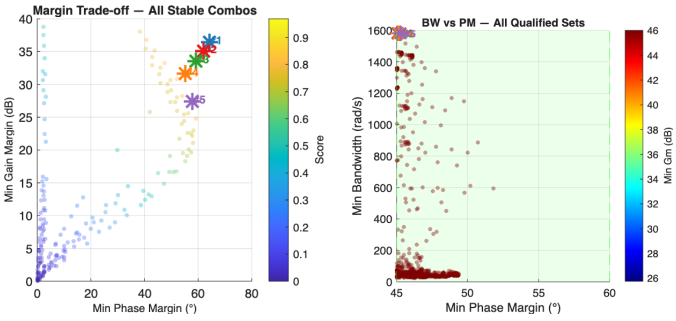

Fig. 4. Left: worst-case gain/phase-margin trade-off over all Routh-feasible tunings for the robustness optimization (11). Right: worst-case bandwidth versus worst-case phase margin for the performance optimization (12). In both panels, the top-5 candidates are highlighted.

D. Design Guidelines

The numerical study supports the following practical guidelines.

1) *Choose the control allocation gain M_d and the controller gain k_p jointly, and guarantee the correct sign of M_d.* Sweep A shows that the admissible k_p ceiling increases as M_d moves from large-magnitude values toward zero while preserving the nominal sign, but vanishes abruptly when M_d crosses zero. A sign error in M_d is therefore the most dangerous failure mode: it reverses the allocation feedback and makes stabilization with any positive k_p impossible.
2) *Keep τ_δ and $I_{yy,c}$ near their nominal values at nominal gain, or reduce k_p accordingly.* Sweep B shows that simultaneously driving τ_δ and $I_{yy,c}$ toward 0% of nominal destabilizes the loop by collapsing the fifth-order polynomial structure: $\tau_\delta \to 0$ removes the highest-order dynamic term $C_5 = \tau_{\mathrm{act}}\tau_q\tau_\delta$, while $I_{yy,c} \to 0$ weakens the low-order gain-carrying terms through $G_{MM} \to 0$. At very small k_p this mechanism is much less severe, which is why the robustness-optimal set can combine small τ_δ and $I_{yy,c}$ with $k_p \approx 0$. At nominal or high k_p, the matched values $\tau_\delta = \tau_{\mathrm{act}}$ and $I_{yy,c} = I_{yy,m}$ should be respected.
3) Use the $d_q = 0$ design as a conservative linear baseline when aerodynamic damping is uncertain. A tuning that is stable at $d_q = 0$ is therefore an appropriate conservative starting point when the true damping is not known accurately.
4) *Validate the performance-optimal solution within its uncertainty bounds.* The performance-optimal solution in Section IV-B is derived under $d_q > 0$ and therefore requires knowledge of the *nominal* value of d_q, not its exact value; the $\pm 10\%$ uncertainty margin on d_q demonstrates that moderate uncertainty in the damping estimate is tolerable. The step responses in Fig. 3 confirm the improved bandwidth for all evaluated corners, but the result should not be extrapolated beyond the tested uncertainty range or to operating points where d_q is poorly characterized.

V. Conclusion

This paper presented a systematic linear stability analysis of an INDI pitch-rate controller for a tilt-rotor VTOL UAV under model mismatch. A closed-form fifth-order transfer function was derived and the Routh–Hurwitz criterion was used to characterize stability regions in two three-parameter subspaces. The stability volumes reveal that actuator lag and inertia mismatch are less destabilizing than control-effectiveness mismatch over the displayed sweep ranges: large M_d combined with large k_p collapses the gain-dependent Routh coefficients, and a sign error in M_d eliminates all positive-gain stability abruptly. Two uncertainty-aware tuning procedures were formulated and solved, providing concrete recommendations for robustness-priority and performance-priority conditions together with a quantification of the resulting speed–robustness trade-off.

Within the parameter range considered here, the $d_q = 0$ baseline is conservative: positive aerodynamic damping shifts the coefficient set in a stabilizing direction and did not tighten the observed stability boundary. Large-amplitude maneuvers, trim-point shifts during transition, and actuator saturation introduce nonlinear effects that can change effective gain and phase lag, thereby tightening or shifting the Routh boundary derived here. Future work will extend the stability certificate to this nonlinear saturated regime via Sum-of-Squares Lyapunov methods [12], enabling certified stability regions that account for actuator saturation directly. In addition, while the pitch focus is motivated by the longitudinal transition mechanism discussed in Section I, a more complete full-envelope certificate should include roll/yaw coupling for asymmetric actuation, lateral disturbances, and non-longitudinal maneuvers.

References

[1] E. J. Smeur, Q. Chu, and G. C. de Croon, "Adaptive incremental nonlinear dynamic inversion for attitude control of micro air vehicles", *J. Guid. Control Dyn.*, vol. 39, no. 3, pp. 450–461, 2016.

[2] M. Schlatter, G. Ducard, D. Rohr, and C. Onder, "Longitudinal control of a tilt-rotor VTOL UAV using incremental nonlinear dynamic inversion", in *Proc. IEEE Int. Conf. Control Autom. Diagnosis (ICCAD)*, 2024.

[3] E. Tal and S. Karaman, "Global incremental flight control for agile maneuvering of a tailsitter flying wing", *J. Guid. Control Dyn.*, vol. 45, no. 12, pp. 2332–2349, 2022.

[4] G. Ducard, H. P. Geering, "Stability Analysis of a Dynamic Inversion Based Pitch Rate Controller for an Unmanned Aircraft", Proceedings of the IEEE/RSJ 2008 Int. Conf. on Intelligent Robots and Systems (IROS), pp. 360-366, France, September 2008. https://doi.org/10.1109/IROS.2008.4651117

[5] G. Ducard, H. P. Geering, "Airspeed Control for Unmanned Aerial Vehicles: a Nonlinear Dynamic Inversion Approach" Proceedings of the 16th IEEE Mediterranean Conference on Control and Automation (MED), pp. 676-681, France, June 2008. https://doi.org/10.1109/MED.2008.4602202

[6] G. Ducard, "Fault-Tolerant Flight Control and Guidance Systems: Practical Methods for Small Unmanned Aerial Vehicles", Springer, 2009.

[7] A. Steinert, S. Raab, S. Hafner, F. Holzapfel, and H. Hong, "Advancements in incremental nonlinear dynamic inversion and its components: A survey on INDI – Part II", *Chinese J. Aeronaut.*, vol. 38, no. 11, p. 103591, 2025.

[8] C. Park, A. Ramirez-Serrano, and M. Bisheban, "Adaptive incremental nonlinear dynamic inversion control with guaranteed stability for aerial manipulators", *Aerospace*, vol. 12, no. 4, p. 312, 2025.

[9] R. van't Veld, E. van Kampen, and Q. Chu, "Stability and robustness analysis and improvements for incremental nonlinear dynamic inversion control", in *AIAA SciTech Forum*, 2018.

[10] X. Wang, E. J. van Kampen, Q. P. Chu, and P. Lu, "Stability analysis for incremental nonlinear dynamic inversion control", *J. Guid. Control Dyn.*, vol. 42, no. 5, pp. 1116–1129, 2019.

[11] G. F. Franklin, J. D. Powell, and A. Emami-Naeini, "Feedback Control of Dynamic System", 6th ed. Pearson, 2006.

[12] A. Detailleur, D. Wahby, G. Ducard, C. Onder, "Contributions to Semialgebraic-Set-Based Stability Verification of Dynamical Systems with Neural-Network-Based Controllers", arXiv:2510.24391v1, 2025